Accepted for publication in *Nature Astronomy* published by Springer Nature. Available at: 10.1038/s41550-019-0832-x

High Porosity Boulders Identified on C-type Asteroid (162173) Ryugu

M. Grott, J. Knollenberg, M. Hamm, K. Ogawa, R. Jaumann, K. Otto, M. Delbo, P. Michel, J. Biele, W. Neumann, M. Knapmeyer, E. Kührt, H. Senshu, T. Okada, J. Helbert, A. Maturilli, N. Müller, A. Hagermann, N. Sakatani, S. Tanaka, T. Arai, S. Mottola, S. Tachibana, I. Pelivan, L. Drube, J.-B. Vincent, H. Yano, C. Pilorget, K. D. Matz, N. Schmitz, A. Koncz, S. Schröder, F. Trauthan, M. Schlotterer, C. Krause, T.-M. Ho, A. Moussi-Soffys

C-type asteroids are among the most pristine objects in the solar system, but little is known about their interior structure and surface properties. Telescopic thermal infrared observations have so far been interpreted in terms of a regolith covered surface with low thermal conductivity and particle sizes in the centimeter range. This includes observations of C-type asteroid (162173) Ryugu, for which average grainsizes of 3-30 mm have been derived[1,2,3]. However, upon arrival of the Hayabusa2 spacecraft at Ryugu, a regolith cover of sand- to pebble-sized particles was found to be absent[4,5]. Rather, the surface is largely covered by cobbles and boulders, seemingly incompatible with the infrared observations. Here we report on the first in-situ thermal infrared observations of a boulder on a C-type asteroid. Boulder thermal inertia was found to be much lower than anticipated based on laboratory measurements of meteorites, which implies that the boulder itself exhibits low thermal conductivity. Our results furthermore indicate high boulder porosities as well as a low tensile strength in the few hundred kPa range. This confirms the suspected observational bias in our meteorite collections, as typical samples of common asteroid types would be too frail to survive atmospheric entry.

On October 3rd, 2018, the Hayabusa2 spacecraft[6] delivered the MASCOT[7] lander to the surface of asteroid (162173) Ryugu, where MASCOT's infrared radiometer MARA[8] obtained surface brightness temperature measurements for a full day-night cycle. The instrument's field of view covered a spot of approximately 10 cm in diameter on the surface, which was also observed by MASCOT's optical camera MasCam[4]. The scene observed by MARA and MasCam[4] is shown in **Figure 1**, with the footprint of the MARA 8-12 μm broadband sensor indicated in red. MARA is viewing the top face of a slightly raised (~3 cm) boulder in front of MASCOT. The boulder is rough in surface texture at the sub-centimeter scale and generally appears angular to sub-angular.

Particles with diameters larger than 0.6 mm are resolvable at the bottom of the image (~0.2 mm per pixel resolution), but only a few separate roundish grains can be identified as loose grains on this formation. Furthermore, an optically thick cover of fine particles is not observed, and bright inclusions are visible at multiple locations including the area viewed by MARA. Highly resolved areas in the MasCam image show that the boulder is composed of a relatively dark matrix with mostly bright but also darker inclusions at the millimeter scale[4].

Remote spectral observations of Ryugu suggest a composition similar to heated CM (CM2) or CI meteorites[9]. However, the texture observed in close-up images (compare Fig. 1) shows millimeter-sized inclusions in at least one location and bright speckles at varying distances. This seems to be incompatible with a CM2 composition, for which petrographic analysis[10] shows maximum grain sizes around 0.2 mm. On the other hand, CI meteorites are predominantly composed of a fine-grained matrix with a mottled appearance, and the texture observed by MASCOT resembles that of the rare CI2 Tagish Lake meteorite, which possesses up to 2 mm large calcium aluminum rich inclusions[11]. Thus, CI2 type meteorites appear to be the closest known Ryugu analogue. However, as Tagish Lake is a rare sample and variations in inclusion sizes are common for carbonaceous chondrites, it is not feasible to derive a definite meteorite analogue. Rather, it may be possible that the investigated boulder is not represented in any meteorite collection on Earth.

Temperatures measured using MARA's 8-12 μm filter are shown as a function of local time in Figure 2a along with the best-fitting thermal models taking the illumination conditions at the landing site as well as surface roughness into account (see methods). Diurnal temperatures rise steeply in the morning, but start dropping around 11:07 local time, indicating shadows passing through the radiometer field of view before noon. Maximum temperatures reach 308 K shortly after local noon and the sun sets at 16:39 local time. The complex shape of the daytime temperature curve indicates a rough surface, consistent with camera observations. During nighttime, temperatures drop to 201 K.

As daytime data is affected by surface roughness and re-radiation from the environment, only equilibrated nighttime temperatures are used to fit thermophysical models. Best-fitting models (see methods) are indicated in Figure 2a and correspond to a thermal inertia Γ of 282 J m^{-2} K^{-1} $s^{-1/2}$. While fitting nighttime data perfectly, the steep increase of temperature during the morning is underestimated, while midday temperatures are overestimated. Taking surface roughness into account (green solid line in Figure 2a), the quality of the fit to midday temperatures is much improved, but early morning temperatures cannot be fit using this model. The latter are influenced by light reflected from the MASCOT lander, and a local terrain model including reflections would be necessary to improve results. Nevertheless, since only equilibrium nighttime temperatures are used to estimate the thermal inertia Γ, presented results are largely independent of surface roughness and topography.

Admissible thermal inertia values are shown as a function of maximum insolation in Figure 2b, where the orientation of the surface normal has been systematically varied around its nominal value. The color bar shows the χ^2 of the individual fits, and emissivity has been varied between 0.9 and 1. Low Γ corresponds to low emissivity and models with and without re-radiation have been considered. As a result, admissible thermal inertia values for the boulder in the MARA field of view were found to be 282^{+93}_{-35} J m^{-2} K^{-1} s$^{-1/2}$. This estimate is similar to telescopically determined thermal inertia values[1] of 150 to 300 J m^{-2} K^{-1} s$^{-1/2}$ and values determined by the thermal infrared imager on the Hayabusa2 spacecraft[5], which range from 200 to 500 J m^{-2} K^{-1} s$^{-1/2}$. It therefore seems likely that boulders dominate the thermal emission from Ryugu, which would be consistent with the high rock abundance determined from orbiter images[5]. Therefore, contrary to expectation, the low thermal inertia derived for Ryugu does not correspond to a pebble-sized regolith-covered surface[1,2]. Rather, boulder to block-sized clasts themselves appear to have thermal inertia lower than that of CM2 Cold Bokkeveld, which has the lowest thermal inertia (600 - 700 J m^{-2} K^{-1} s$^{-1/2}$) of a meteorite measured so far.

While thin layers of fine material could in principle mask the thermal signature of competent rock, the boulder observed by MARA appears to be free from an optically thick, dusty layer. Furthermore, the presence of a fine dust layer can be ruled out by considering a two layer thermal model. Results of the calculations (see methods) are shown in Figure 3, where dust with a thermal inertia of 25 J m^{-2} K^{-1} s$^{-1/2}$ was assumed to cover a boulder with a thermal inertia of 700 J m^{-2} K^{-1} s$^{-1/2}$. As is evident, the model is incompatible with the observed nighttime cooling rates, and the boulder observed by MARA itself must exhibit very low bulk thermal conductivity to fit the data. However, it cannot be ruled out that the low conductivity zone is limited to a highly porous outer layer. Such a layer may for example be generated by cracking due to thermal fatigue[12,13,14] and could extend to a few thermal skin depths.

Given the above estimate of thermal inertia, thermal conductivity can be derived for a given bulk density and heat capacity (see methods). Furthermore, since thermal conductivity k of porous material depends more on porosity ϕ, and thus the total area of inter-grain contacts, than on the conductivity of the grains themselves[3], the porosity of the investigated boulder could in principle be estimated if the functional dependence of $k(\phi)$ were known. However, while models for H and L chondrites indicate that porosity and thus thermal conductivity is governed by dehydration- or shock-induced cracks[15,16,17], thermal conductivity data on CI chondrites are absent. Nevertheless, since cracks are abundant in CI types[18], it stands to reason that a similar mechanism would reduce thermal conductivity in these types and models derived for H and L chondrites should be applicable to CI types, too.

Two models[16,17] for thermal conductivity as a function of porosity are shown in Figure 4a. Available data for H, L, and CM chondrites are shown together with the thermal conductivities extrapolated for Ryugu. The first model[16] results in $28 < \phi < 34\%$, typical for CM and CI chondrites, which have class average porosities of 22.2% and 34.9%, respectively[17]. The second model[17] yields $41 < \phi < 55\%$. Other models applicable to partially-sintered granular material[16] yield intermediate results. Corresponding thermal conductivities are 0.06 - 0.13 and 0.09 – 0.16 W m^{-1} K^{-1}, respectively, and thus much lower than measurements reported for the thermal conductivities of meteorites. Measurements on CI chondrites are missing entirely, but since CI chondrites are those meteorites with highest porosities[17], low conductivities could be expected.

Pores in the boulder would be observable in nighttime images, as the illumination provided by the MasCAM LED array covers a variety of directions. However, no such pores are observed, indicating that potential pores must be smaller than 1 mm. The radiative contribution to the total heat transport inside the boulder can now be estimated by considering radiative heat exchange between parallel planes[3], and for pores smaller than 1 mm this results in a minor contribution to the overall thermal conductivity. The latter must therefore be governed by solid conduction through grain contacts. Given porosity and thermal conductivity, the amount of contacts can be estimated, which in turn can be converted to an estimate of tensile strength (see methods). Given the values derived above and assuming a Young's modulus representative for carbonaceous chondrites, tensile strength of the boulder is estimated to be 200 to 280 kPa and thus considerably lower than measurements on meteorite samples[17], which generally show tensile strengths of the order of one to a few MPa[19]. This low tensile strength indicates an observational bias, namely that any hypothetical meteoroid originating from the boulder observed by MASCOT would likely break up during atmospheric entry and would thus be absent in our meteorite collections.

Thermal conductivity values derived above can be compared to estimates for other minor bodies, and corresponding data are shown in Figure 4b, where thermal conductivity is given as a function of temperature for asteroids (162173) Ryugu[1], (101955) Bennu[20], and the average estimated for small near Earth asteroids[21]. Values are compatible within error bars and similar to values derived for comets 67P/Churyumov–Gerasimenko[22], 9P/Tempel 1[23,24], and 103P/Hartley 2[23] when heat capacity is properly scaled for temperature and appropriate densities are assumed (see methods section). On the other hand, estimates for S-type asteroid (25143) Itokawa[25,26] are larger by a factor of three, indicating that thermal properties of C-type asteroids are more similar to those of comets than those of S-type asteroids. It is also worth noting that no cubic dependence of thermal conductivity on temperature is observed in Figure 4b, which could indicate that radiative heat transfer through large pores is negligible in the bodies considered here.

The high porosities derived here have important implications for Ryugu's parent body. Assuming initial porosities[27] of the order of 70%, the Ryugu precursor needs to have been large enough to reduce intrinsic (micro-) porosity to values below 55% by compaction and aqueous alteration, while simultaneously avoiding porosities to drop below 28%. This implies that the material we observe on Ryugu's surface today was either produced in the outer layers of a larger (50-100 km sized) parent body, or the interior of a smaller, kilometer-sized body. The latter would be feasible provided accretion occurred while ^{26}Al was still active, in which case aqueous alteration and hot pressing of the precursor material would be efficient. In this way, porosities of 45% can be achieved starting from initial porosities of 70% even on small, kilometer-sized objects, provided that a water ice dominated primordial composition similar to that of CI/CM chondrites is assumed[28,29].

References

1. Wada, K., Grott, M., Michel, P., Walsh, K., *et al.*, Asteroid Ryugu Before the Hayabusa2 Encounter, *Progress Earth Plan. Sci.*, 5:82, doi:10.1186/s40645-018-0237-y (2018).
2. Gundlach, B., Blum, J., A new method to determine the grain size of planetary regolith, *Icarus* 223, 479–492, doi:10.1016/j.icarus.2012.11.039 (2013).
3. Sakatani, N., Ogawa, K., Iijima, Y., Arakawa, M., Honda, R., Tanaka, S., Thermal conductivity model for powdered materials under vacuum based on experimental studies, *AIP Advances* 7, 015310 (2017).
4. Jaumann, R., Schmitz, N., Ho, T.-M. Schröder, S., Otto, K., *et al.*, In-situ investigation of asteroid (162173) Ryugu by the Mobile Asteroid Surface Scout (MASCOT) Camera (MASCam), *Science*, submitted.
5. Sugita, S., Honda, R. Morota, T., *et al.*, The geomorphology, color, and thermal properties of Ryugu: Implications for parent-body processes, *Science*, 364, 252 (2019).
6. Watanabe, S., Tsuda, Y., Yoshikawa, M., *et al.*, Hayabusa2 Mission Overview, *Space Sci. Rev*. 208: 3, doi:10.1007/s11214-017-0377-1 (2017).
7. T.M. Ho, V. Baturkin, C. Grimm, *et al.*, MASCOT—The Mobile Asteroid Surface Scout Onboard the Hayabusa2 Mission, *Space Sci. Rev.* 208: 339, doi.org/10.1007/s11214-016-0251-6 (2017).
8. Grott, M., Knollenberg, J., Borgs, B., *et al.,* The MASCOT Radiometer MARA for the Hayabusa 2 Mission. *Space Sci. Rev.* 208: 413, doi:10.1007/s11214-016-0272-1(2017).
9. Moskovitz, N.A., Abe, S., Pan, K.-S.,.Osip, D.J, Pefkou, D., Melita, M.D., Elias, M., Kitazato, K., Bus, S.J., DeMeo, F.E., Binzel, R.P., Abell, P.A., Rotational characterization of Hayabusa II target Asteroid (162173) 1999 JU3, *Icarus* 224, 24–31 (2013).
10. King, T.V.V., King, E.A., Grain Size and Petrography of C2 and C3 Carbonaceous Chondrites, *Meteoritics* 13, 47–72 (1978).
11. Brown, P.G., Hildebrand, A.R., Zolensky, M.E., Grady, M., Clayton, R.N., Mayeda, T.K., Tagliaferri, E., Spalding, R., MacRae, N.D., Hoffman, E.L., Mittlefehldt, D.W., Wacker, J.F., Bird, J.A., Campbell, M.D., Carpenter, R., Gingerich, H., Glatiotis, M., Greiner, E., Mazur,

M.J., McCausland, P.J., Plotkin, H., Mazur, T.R., 2000. The Fall, Recovery, Orbit, and Composition of the Tagish Lake Meteorite: A New Type of Carbonaceous Chondrite, *Science,* 290, 320–325, (2000).

12. Delbo, M., Libourel, G., Wilkerson, J., Murdoch, N., Michel, P., Ramesh, K.T., Ganino, C., Verati, C., Marchi, S., Thermal fatigue as the origin of regolith on small asteroids., *Nature*, 508(7495):233-6 (2014).
13. Hamm, M., Senshu, H., Grott, M., Latitudinal Dependence of Asteroid Regolith Formation by Thermal Fatigue, *Plan. Space Sci.*, doi:10.1016/j.icarus.2018.09.033 (2018).
14. Molaro, J.L., Byrne, S., Le, J.-L., Thermally induced stresses in boulders on airless body surfaces, and implications for rock breakdown, *Icarus*, 294, 247-261 (2017).
15. Krause, M., Blum, J., Skorov, Yu.V., Trieloff, M., Thermal conductivity measurements of porous dust aggregates: I. Technique, model and first results, *Icarus* 214, 286–296, doi:10.1016/j.icarus.2011.04.024 (2011).
16. Henke, S., Gail, H.-P., Trieloff, M., Thermal evolution and sintering of chondritic planetesimals III. Modelling the heat conductivity of porous chondrite material, *Astron. Astrophys.* 589, A41 (2016), doi: 10.1051/0004-6361/201527687 (2016).
17. Flynn, G.J., Consolmagno, G.J., Brown, P., Macke, R.J., Physical properties of the stone meteorites: Implications for the properties of their parent bodies, *Chemie der Erde* 78, 269–298, doi:10.1016/j.chemer.2017.04.002 (2018).
18. Tonui, E., Zolensky, M., Hiroi, T., Nakamura, T., Lipschutz, M.E., Wang, M.-S., Okudaira, K. Petrographic, chemical and spectroscopic evidence for thermal metamorphism in carbonaceous chondrites I: CI and CM chondrites, *Geochim. et Cosmochim. Acta* 126, 284–306 (2014).
19. Ostrowski, D., Bryson, K., The physical properties of meteorites, *Planetary and Space Science*, 165, 148-178 (2019).
20. DellaGiustina, D.N., Emery, J.P., Golish, D.R., et al., Properties of rubble-pile asteroid (101955) Bennu from OSIRIS-REx imaging and thermal analysis, *Nature Astronomy*, doi: 10.1038/s41550-019-0731-1

21. Delbo, M., dell'Oro, A., Harris, A.W., Mottola, S., Mueller, M. ,Thermal inertia of near-Earth asteroids and implications for the magnitude of the Yarkovsky effect, *Icarus* 190, 236–249 (2007).
22. Spohn, T., Knollenberg, J., Ball, A.J., et al., Thermal and mechanical properties of the near-surface layers of comet 67P/Churyumov-Gerasimenko, *Science* 349: 6247 (2015).
23. Groussin, O. *et al.*, The temperature, thermal inertia, roughness and color of the nuclei of Comets 103P/Hartley 2 and 9P/Tempel, *Icarus* 222, 580–594 doi: 10.1016/j.icarus.2012.10.003 (2013).
24. Davidsson, B. J. R., Gutiérrez, P. J., Rickmann, H., Physical properties of morphological units on comet 9P/Tempel 1 derived from near-IR Deep Impact spectra, *Icarus* 201, 335–357 doi: 10.1016/j.icarus.2008.12.039 (2009).
25. Fujiwara, A., Kawaguchi, J., Yeomans, D.K., Abe, M., *et al.*, The Rubble-Pile Asteroid Itokawa as Observed by Hayabusa, *Science* 312: 1330-1334 (2006).
26. Müller, T.G., Hasegawa, S., Usui, F., (25143) Itokawa: The power of radiometric techniques for the interpretation of remote thermal observations in the light of the Hayabusa rendezvous results, *Publ. Astron. Soc. Japan* 00 (0), 1–17, doi: 10.1093/pasj/psu034 (2014).
27. Yang, R.Y., Zou, R.P., Yu, A.B., Computer simulation of the packing of fine particles, *Physical Review E*, 62(3), 3900–3908. doi:10.1103/physreve.62.3900 (2000).
28. Neumann, W., Breuer, D., Spohn, T., On the modelling of compaction in planetesimals, *Astr. Astrophys.*, 567, A120, doi:10.1051/0004-6361/201423648 (2014).
29. Neumann, W., Breuer, D., Spohn, T., Modelling the internal structure of Ceres: Coupling of accretion with compaction by creep and implications for the water-rock differentiation. *Astron. Astrophys.*, 584, A117, doi:10.1051/0004-6361/201527083 (2015).

Correspondence and requests for materials should be addressed to Matthias Grott (Matthias.Grott@dlr.de)

Acknowledgments

The MASCOT lander on the Hayabusa2 Mission of JAXA is a DLR/CNES cooperation. MASCOT MARA has been developed and built under the leadership of the DLR Institute of Planetary Research with contracted contributions from the Institute of Photonic Technology. The Hayabusa2 Mission is operated by JAXA. **Funding:** K.O. acknowledges funding by the JSPS Core-to-Core Program "International Network of Planetary Sciences." A.H. acknowledges funding by STFC under grant no. ST/S001271/1.

Author contributions

M.G. coordinated and wrote the paper, J.K. and M.G. evaluated the instrument calibration, M.H., K.O., S.M., J.-B.V., M.S. and I.P. computed illumination and thermal models, N.S., S.S., A.K. and F.T. contributed to camera development, K.O. and K.D.M. localized the MARA FoV in camera images, W.N., P.M., S.T., J.B., M.D., and M.K. provided the discussion on material parameters, H.S., T.O., E.K., J.B., H.Y., R.J., N.M., C.P., L.D., N.S., S.T., T.A., and S.S. added to the science discussion, J.H. and A.M. contributed to the radiometer development, C.K., T.-M.H., and A.M.-S. contributed to data acquisition. A.H. contributed to instrument characterization. All authors have read and approved the final manuscript.

Author Information:

M. Grott (Correspondence to: Matthias.Grott@dlr.de.), J. Knollenberg, M. Hamm, R. Jaumann, K., M. Knapmeyer, E. Kührt, K. Otto, J. Helbert, A. Maturilli, N. Müller, S. Mottola, L. Drube, J.-B. Vincent, K. D. Matz, N. Schmitz, A. Koncz, S. Schröder, F. Trauthan, German Aerospace Center (DLR), Berlin, Germany.

K. Ogawa, Department of Planetology, Graduate School of Science, Kobe University, Kobe, Japan

M. Delbo, P. Michel, Université Côte d’Azur, Observatoire de la Côte d'Azur, CNRS, Laboratoire Lagrange, Nice, France

J. Biele, German Aerospace Center (DLR), Cologne, Germany

W. Neumann, Institut für Planetologie, University of Münster, Münster, Germany

H. Senshu, Planetary Exploration Research Center, Chiba Institute of Technology, Narashino, Japan

T. Okada, N. Sakatani, S. Tanaka, H. Yano, Institute of Space and Astronautical Science, Japan Aerospace Exploration Agency, Sagamihara, Japan.

A. Hagermann, University of Stirling, Stirling, UK

T. Arai, Division of System and Information Engineering, Ashikaga University, Tochigi, Japan.

S. Tachibana, UTokyo Organization for Planetary and Space Science, University of Tokyo, Japan.

I. Pelivan, Institute of Mathematics, University of Potsdam, Germany, and Fraunhofer Heinrich Hertz Institute (HHI), Berlin, Germany

C. Pilorget, Institut d'Astrophysique Spatiale, Université Paris Sud, Orsay, France

M. Schlotterer, T.-M. Ho, German Aerospace Center (DLR), Bremen, Germany.

C. Krause, German Aerospace Center (DLR), Cologne, Germany.

A. Moussi-Soffys, Centre National d'Etudes Spatiales (CNES), France.

Figure Legends:

Figure 1: MasCam Image of the boulder observed by MASCOT indicating the MARA field of view (red shaded area). a) The location in daylight (local time 9:20) with the yellow arrow indicating the approximate direction of illumination with sun elevation and azimuth at 40.2° and 67.2°. The image suggests that MASCOT is located in front of an angular to sub-angular formation whose edges are outlined by the yellow dotted line. The yellow dashed line indicates the edge of an elevated part of the boulder (compare the nighttime image on the right). The front face of the formation orientated towards MARA is approximately 3 cm above the plane MASCOT is located on. b) The same location at night (local time 23:18) illuminated by the camera's red LED. Only the foreground is visible due to the limited illumination provided. The images are distorted with pixel resolutions varying between approximately 0.2 mm at the bottom

and 3 mm near the horizon. . Note that due to a minor relocation of MASCOT the scene in panel b) is slightly shifted towards the left with respect to panel a).

Figure 2: Observed and modeled surface temperatures and derived thermal inertia. a) Variation of surface temperature observed in-situ at geographical coordinates of 22.22 ± 0.05°S, 317.26 ± 0.07°E. Temperature is shown as a function of time as derived from the MARA 8-12 µm filter and using a surface emissivity of $\varepsilon = 1$. Error bars indicate 2σ confidence limits and uncertainties are below 0.5 K and 1.5 K during daytime and nighttime, respectively. Data are shown together with best fitting thermal models. While the model shown as a dashed red line assumes a flat surface, midday temperatures are reduced by surface roughness effects for the model shown in green. The steep rise of morning temperatures is caused by reflections from the MASCOT lander (not modeled). Best fitting models correspond to a thermal inertia of 282 J m^{-2} K^{-1} $s^{-1/2}$ and a crater density of 0.34 (see methods). b) Retrieved thermal inertia as a function of the maximum insolation for the respective surface orientation. Emissivity has been varied between $\varepsilon = 0.9$ and 1. The χ^2 value of the individual fits is shown in color and admissible thermal inertia values were found to be 282^{+93}_{-35} J m^{-2} K^{-1} $s^{-1/2}$.

Figure 3: Modeled temperatures for a dust covered surface. Variation of surface temperature as a function of time as derived from the MARA 8-12 µm filter and using a surface emissivity of $\varepsilon = 1$. Error bars indicate 2σ confidence limits and uncertainties are below 0.5 K and 1.5 K during daytime and nighttime, respectively. Data are shown together with the results of a two layer thermal model, which assumes best fitting illumination conditions as well as a thin dust layer covering the underlying boulder. Dust thermal inertia is assumed to be 25 J m^{-2} K^{-1} $s^{-1/2}$. Results for four different dust thicknesses assuming a boulder thermal inertia of 700 J m^{-2} K^{-1} $s^{-1/2}$ are shown.

Figure 4: Derived thermal conductivity and boulder porosity. a) Thermal conductivity as a function of porosity. Data for H, L, and CM chondrites is shown together with two models fitting the data for porosities below 20%. For the low thermal conductivities determined from MARA measurements, models have to be extrapolated to high porosities. Depending on the model used, porosities between 28-34% and 41-55% are obtained. b) Thermal conductivity as a function of temperature as derived for different small bodies. For the boulder in the MARA field of view, a

grain density of 2420 kg m^{-3} has been assumed. Heat capacity[1] was evaluated at 230 K, corresponding to the average observed nighttime temperature. In addition, conductivity values as derived from disc integrated measurements of Ryugu, disc integrated measurements of asteroid Bennu[20], as well as the estimated average thermal conductivity for near Earth asteroids (NEA)[21] are shown. As a comparison, conductivity derived from in-situ observations of comet 67P/Churyumov–Gerasimenko[22] as well as values derived from spacecraft observations of comets 9P/Tempel 1[23,24] and 103P/Hartley 2[23] are given. In contrast, the conductivity derived from disc integrated measurements of asteroid Itokawa[26] is also shown.

Methods

Asteroid Thermophysical Model. To estimate thermophysical properties from the brightness temperatures observed, a thermophysical model of the Ryugu boulder was constructed assuming a single, flat surface in the MARA field of view. A specific heat c_p of 600 J kg^{-1} K^{-1} and density ρ of 1270 kg m^{-3} have been assumed for the boulder, consistent with pre-encounter estimates[1]. Parameters have been assumed to be constant and independent of temperature, as more complicated models did not improve the quality of the fit. Thermal conductivity k was treated as a free fitting parameter, and results are reported in terms of surface thermal inertia

$$\Gamma = \sqrt{k\rho c_p} \tag{1}$$

Insolation of the surface in the field of view was varied around the average surface normal which, according to the Ryugu shape model, points towards longitude 314.207°E and latitude 34.599°S in the asteroid fixed frame at the landing site. In a local frame, elevation and azimuth of the normal vector have been varied by 25° and 360° around this surface normal, respectively. This accounts for the unknown orientation of the surface in the MARA field of view and covers all plausible illumination conditions. Results are reported in terms of the maximum insolation corresponding to the respective surface normal. Furthermore, the times of sunrise and sunset have been adapted to fit MARA observations, which indicate that sunrise is delayed by 37 min with respect to the nominal insolation. In addition, the sun sets 21 min earlier than predicted by the illumination model and insolation has been adapted accordingly. This is consistent with the terrain at the landing site, which shows that MASCOT is situated in a local depression.

Re-radiation from the environment onto the surface observed by MARA was taken into account using a local terrain model. View factors *f* from the surrounding topography to the surface have been estimated from the model and were found to amount to 0.048 ± 0.007 for facets within 1 meter of the MASCOT landing site (see supplementary Figures 1 and 2). No facet showed $f > 0.08$. In the thermophysical modeling, *f* has been varied between 0 and 0.08 to provide a conservative upper limit. The incident flux was then derived assuming that the surrounding terrain has temperatures T_{obs} corresponding to those on the surface of the boulder observed by MARA. As thermal re-radiation decreases the estimated thermal inertia, *f* = 0.08 results in an upper limit for the derived thermal inertia.

Given insolation I and thermal inertia Γ, the 1D heat equation is solved[30] using

$$-\Gamma\sqrt{\frac{\pi}{P}}\frac{\partial T}{\partial z} = (1-A)I - \sigma\varepsilon T^4 + f\sigma\varepsilon T_{obs}^4 \tag{2}$$

as the upper boundary condition. Here, T is surface temperature, Γ thermal inertia, P rotation period, A bond albedo, σ the Stephan-Boltzmann constant, z depth normalized to the diurnal skin depth[31], ε emissivity, and f the view factor to the surrounding environment. In the calculations, an albedo of $A = 0.0146$ is assumed while emissivity was varied between 0.9 and 1. The rotation period of Ryugu is 7.6326 h.

Data Fitting. To avoid complications caused by inhomogeneous temperatures in the MARA field of view due to the changing illumination conditions and re-radiation from the surroundings, only equilibrated nighttime data were used to fit thermophysical models[32] and invert for thermophysical parameters. To fit the data, a suite of models was computed by systematically varying thermal inertia and the orientation of the surface normal in a grid search approach. In the models, thermal inertia was varied in steps of 1 J m^{-2} $\mathrm{s}^{-1/2}$ K^{-1} between 170 and 410, elevation of the target surface normal was varied in steps of 5° between 90° and 65°, and azimuth of the target surface normal was varied in steps of 10° between 0° and 360°. For each model, the χ^2 value between model and data was computed and models resulting in a χ^2 larger than a critical value were discarded. Here we choose a critical χ^2_{crit} corresponding to a 2σ confidence interval[30]

$$0.05 = \int_{\chi^2_{crit}}^{\infty} f(\chi^2, \nu)\, d\chi^2$$

where $f(\chi^2, \nu)$ is the χ^2-distribution and ν is equal to the number of data points minus the number of fitting parameters. We obtain a critical χ^2_{crit} of 587.8 for the 534 data points obtained between 17:15 and 07:16 local time used in the fitting. The minimum χ^2_{min} obtained for the best fit was found to be $\chi^2_{min} = 66$.

This procedure was repeated by varying surface emissivity and assuming values of $\varepsilon = 0.9$, 0.95 and 1. Furthermore, models with view factors to the surroundings of $f = 0$ and 0.08 have been computed to study the effect of re-radiation, which was found to have only a small influence on nighttime temperatures. The stated uncertainty for the thermal inertia was then derived from the lowest and highest admissible values of all simulations. The best-fitting model has an emissivity of $\varepsilon = 1$. For consistency, the emissivity used for both the thermophysical models and the derivation of surface temperature from the observed flux was identical in all cases.

Surface Roughness. For a rough surface, observed flux depends on the solar zenith angle φ, the angle between surface normal and observation direction δ, as well as the angle between projections of the sun vector and the observation direction onto the surface ψ. These need to be taken into account when calculating fluxes received by the instrument. Here, the rough surface is modeled as a surface covered by spherical-section craters[33,34], assuming lateral heat transport to be negligible. Using this model, a factor $c_r(\varphi, \delta, \psi, t, \lambda)$ is calculated for each time t and observed wavelength λ relating the flux emitted by a flat surface F to the flux emitted by the rough surface $F_r = c_r(\varphi, \delta, \psi, t, \lambda)F$. This model is scale-independent[33], leaving the crater density on the surface and the opening angle of the craters as free parameters. The latter is kept constant at 180°, corresponding to a surface covered by hemispherical depressions. The model also depends on parameters such as albedo and heliocentric distance, which are all kept constant to be consistent with the thermophysical model described above. c_r was calculated at $\lambda = 10\ \mu m$.

Two Layer Model. To estimate the possible influence of a low conductivity dust layer on the modeling results, a two layer regolith model assuming geometry parameters corresponding to those of the best fitting one-layer model was calculated. In the model, the dust layer is treated in the continuum approximation, i.e., it is assumed that thermal transport properties inside the layer can be treated using the theory of porous media[3]. This approximation breaks down if thin layers of dust are present, in which case radiative heat transport inside the dust layer would need to be treated explicitly. Here we assume that the dust layer has a thermal inertia of 25 J m^{-2} K^{-1} s$^{-1/2}$. This corresponds to typical particle sizes of ~10 μm at porosities of 80%[3]. Therefore, our model assumptions are valid for layer thicknesses in excess of 50 μm.

Models have then been calculated varying the thermal inertia of the bottom layer along with the top layer thickness. Even thin dust layers appreciably distort the temperature curves, and using bottom layer thermal inertias between 250 and 700 J m^{-2} K^{-1} s$^{-1/2}$, nighttime cooling curves could only be fitted within the errorbars for thermal inertias close to the values reported above. This indicates that the thermophysical properties of the boulder itself govern thermal emission.

Thermal Conductivity and Porosity Estimate. Thermal conductivity k and porosity ϕ for the boulder observed by MARA are calculated by solving

$$k = \frac{\Gamma^2}{c_p \varrho_s (1-\phi)} \tag{3}$$

for a given functional dependence for $k(\phi)$. Here, Γ is thermal inertia, c_p is specific heat, ρ_s is grain density, and ϕ is porosity. For the grain density ρ_s, the average density of CI chondrites[17,35] ρ_s = 2420 kg m^{-3} has been assumed. Heat capacity was determined by evaluating[1] $c_p(T)$ at T = 230 K. For the functional dependence of $k(\phi)$, two models have been considered. Both are based on empirical fits to available thermal conductivity data for chondritic meteorites, and the first relation[17] is

$$k(\phi) = \frac{0.11(1-\phi)}{\phi} \tag{4}$$

while the second relation[16] is

$$k(\phi) = 4.3 e^{-\phi/0.08} \tag{5}$$

Both formulations fit the experimental data equally well, but diverge at porosities larger than 20%.

To compare the thermal conductivity estimates for meteorites with those for comets, cometary thermal inertia estimates have been converted to an estimate of thermal conductivity assuming a cometary bulk density of 300 kg m^{-3} as derived from spacecraft observations[23] of the Deep

Impact experiment on 9P/Tempel 1. For the heat capacity, a value of 1000 J kg^{-1} K^{-1} was used[23]. For the computation of thermal conductivities for (101955) Bennu, (25143) Itokawa, and average NEA, heat capacity[1] was evaluated at a temperature of 340 K, while for the disc-averaged measurement of (162173) Ryugu a temperature of 277 K has been assumed. Assumed bulk densities for (162173) Ryugu[1], average NEA[21], (25143) Itokawa[25], and (101955) Bennu were 1270 kg m^{-3}, 1950 kg m^{-3}, 1950 kg m^{-3}, 1270 kg m^{-3}, respectively.

Strength Estimate. To estimate mechanical tensile strength given thermal conductivity k and porosity ϕ, the amount of inter-grain contacts is estimated neglecting radiative heat transport using[3]

$$k = \frac{4}{\pi^2} k_s (1-\phi) C H \tag{6}$$

where the grain thermal conductivity k_s has been assumed to be 2.95 W m^{-1} K^{-1} as appropriate for serpentine. Here, $H = r_c/R$ is the Hertz factor with r_c being the contact radius and R the radius of interacting spheres. For the coordination number C, the relation

$$C = \frac{2.812(1-\phi)^{-1/3}}{f^2(1+f^2)} \tag{7}$$

was used, where

$$f = 0.07318 + 2.193\phi - 3.357\phi^2 + 3.194\phi^3 \tag{8}$$

Given k, k_s, ϕ, C and H can then be calculated. For a random packing of identical, isotropic and homogeneous spheres with shear modulus μ and Poisson's ratio ν, the bulk elastic parameters can then be related to those in a porous medium following the approach of Digby[36]: in Hertzian contact theory, two identical spheres have a circular contact area of radius r_c, depending on the confining pressure and the Young's modulus of the sphere material. In extension of the Hertz contact model, Digby assumes that the contact area between two spheres contains a small, concentric area of radius $r < r_c$ where the spheres are firmly bonded, i.e., remain in contact even without confining pressure. He obtains the effective Lamé parameters of the packing

$$\lambda_{Digby} = \frac{\mu C(1-\phi)}{5\pi R}\left[\frac{r_c}{1-\nu} - \frac{2r}{2-\nu}\right] \tag{9}$$

$$\mu_{Digby} = \frac{1}{2}\frac{\mu C(1-\phi)}{5\pi R}\left[\frac{2r_c}{1-\nu} + \frac{6r}{2-\nu}\right] \tag{10}$$

We take the adhesive region as a model for a sintering neck between two particles and consider the case without confining pressure, where $r \equiv r_c$. Using the relation

$$E = \mu\frac{3\lambda + 2\mu}{\lambda + \mu} \tag{11}$$

between Lamé-parameters and Young's modulus, and the relation

$$E = 2\mu(1+\nu) \tag{12}$$

between shear modulus, Lamé parameter λ and Young's modulus E, we obtain the effective Young's modulus

$$E_{Digby} = \frac{1}{2\pi}\frac{r_c}{R}C(1-\phi)\frac{1}{1-\nu^2}\frac{5-4\nu}{5-3\nu}E \tag{13}$$

of the conglomerate of sintered spheres in relation to the Young's modulus of the matrix material. Since $0 \leq \nu \leq 1/2$ usually holds for Poisson's ratio, the dependence of E_{Digby} on ν amounts to a factor between 0.988 and $8/7$, or to $256/255 \approx 1.004$ if the matrix material is Poissonian. Therefore, we finally obtain

$$E_{Digby} \cong \frac{1}{2\pi}HC(1-\phi)E = \frac{\pi}{8}\frac{k}{k_s}E \tag{14}$$

and the obtained (reduced) Young's modulus is then converted into an estimate of tensile strength σ_t using the empirical relation[37]

$$\sigma_t = \frac{E_{Digby}}{500} = \frac{\pi}{4000}\frac{k}{k_s}E \tag{15}$$

The Young's modulus E of ordinary chondrites is usually reported[17] to be of the order of tens of GPa, while values for carbonaceous chondrites are usually much lower[38,39], ranging from a few to about 10 GPa. Here we assume 10 GPa to be representative for the Ryugu boulder, pointing out that this likely places an upper limit on the derived tensile strength.

Data Availability

The data that support the plots within this paper and other findings of this study are available from the corresponding author upon reasonable request.

Additional References

30. Hamm, M., Grott, M., Kührt, E., Pelivan, I., Knollenberg, J., A method to derive surface thermophysical properties of asteroid (162173) Ryugu (1999JU3) from in-situ surface brightness temperature measurements, *Plan. Space Sci*. 159, 1-10, doi:10.1016/j.pss.2018.03.017 (2018).
31. Spencer, J.R., Lebofsky, L.A., Sykes, M.V., Systematic biases in radiometric diameter determinations, *Icarus*, 78, 2 (1989).
32. Christensen, P.R., Jakosky, B.M., Kieffer, H.H., *et al.*, The Thermal Emission Imaging System (THEMIS) for the Mars 2001 Odyssey Mission, *Space Science Reviews* 110: 85 (2004).
33. Kuehrt, E., Giese, B., Keller, H. U., Ksanfomality, L. V., Interpretation of the KRFM-Infrared Measurements on Phobos, *Icarus* 96, 213, (1992).
34. Giese, B., Kührt, E., Theoretical Interpretation of Infrared Measurements at Deimos in the Framework of Crater Radiation, *Icarus* 88, 372-379 (1990).
35. Macke, R.J., Consolmagno, G.J., Britt, D.T., Density, porosity, and magnetic susceptibility of carbonaceous chondrites, *Meteoritics & Planetary Science* 46, 1842–1862 (2011).
36. Digby, P.J., The Effective Elastic Moduli of Porous Granular Rocks, *J. Appl. Mechanics* 48, 803-808 (1981).

37. Scholz, C.H., The Mechanics of Earthquakes and Faulting, 2nd Edition, Cambridge Univ. Press (2002)

38. Ibrahim, M. I., The Elastic Properties of Carbonaceous Chondrites, MSc Thesis, Univ. of Calgary, Alberta, http://dx.doi.org/10.11575/PRISM/28122 (2012).

39. Jones, S.F., Elastic Wave Velocity, Porosity, and Pore Geometry of Ordinary Chondrites and Artificially Shocked Samples, MSc Thesis, Univ. of Calgary, Alberta http://dx.doi.org/10.11575/PRISM/22027 (2009).

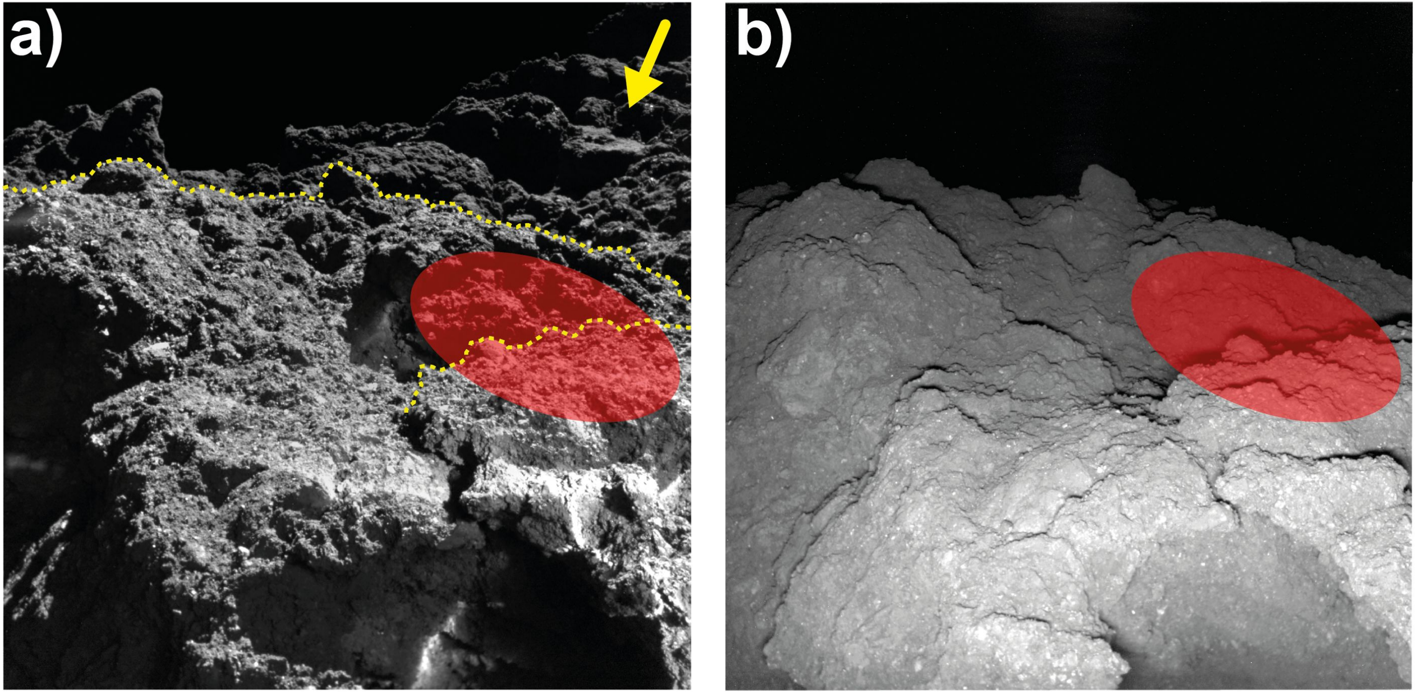
a)
b)

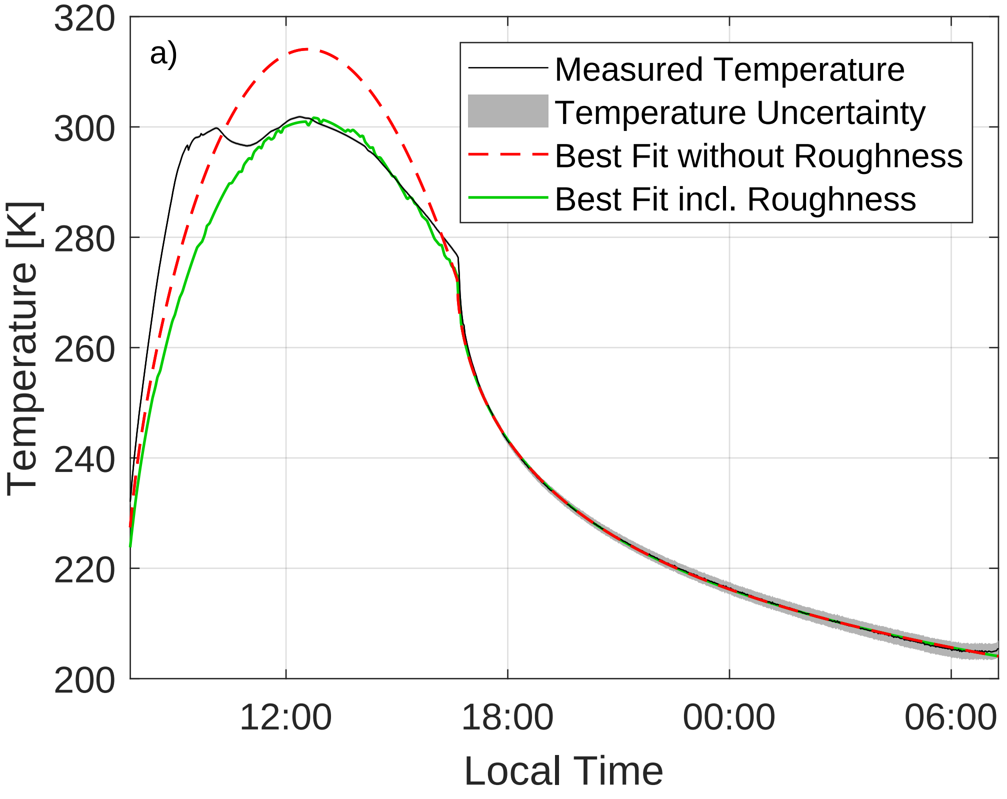
a)
Measured Temperature
Temperature Uncertainty
Best Fit without Roughness
Best Fit incl. Roughness
Temperature [K]
320
300
280
260
240
220
200
12:00
18:00
00:00
06:00
Local Time

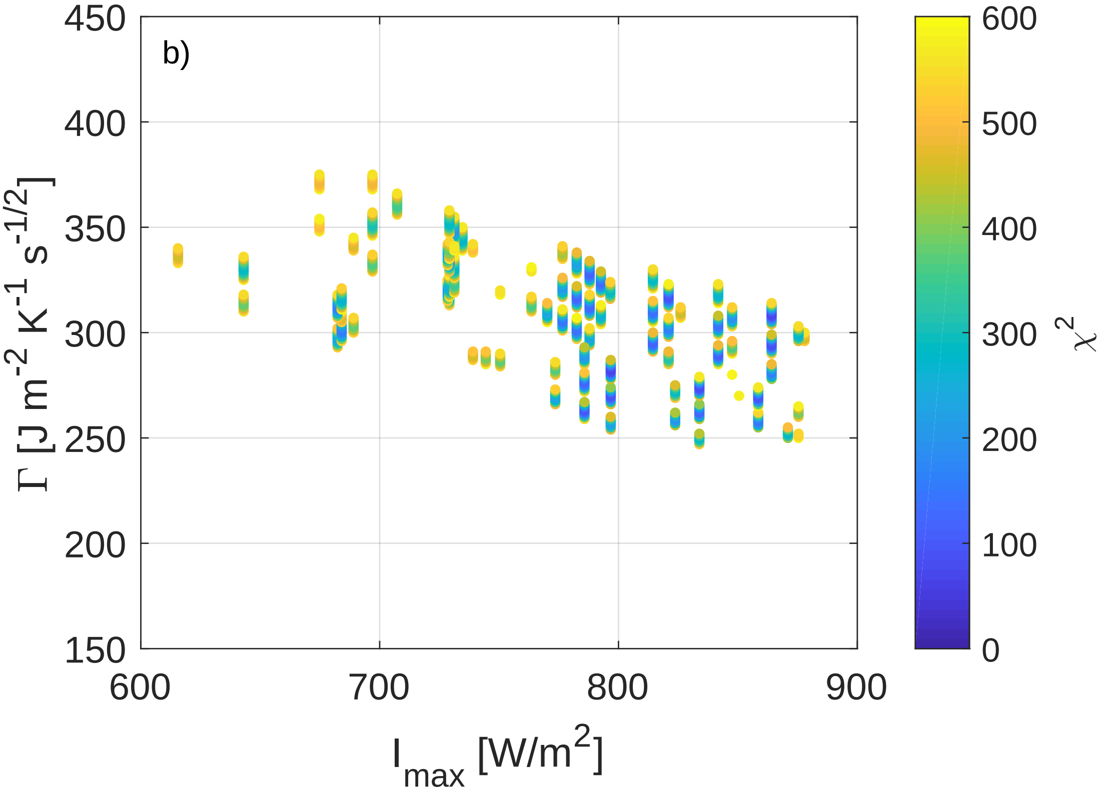
b)
450
400
350
300
250
200
150
600
700
800
900
Γ [J m^{-2} K^{-1} s$^{-1/2}$]
I$_{max}$ [W/m^2]
600
500
400
300
200
100
0
χ^2

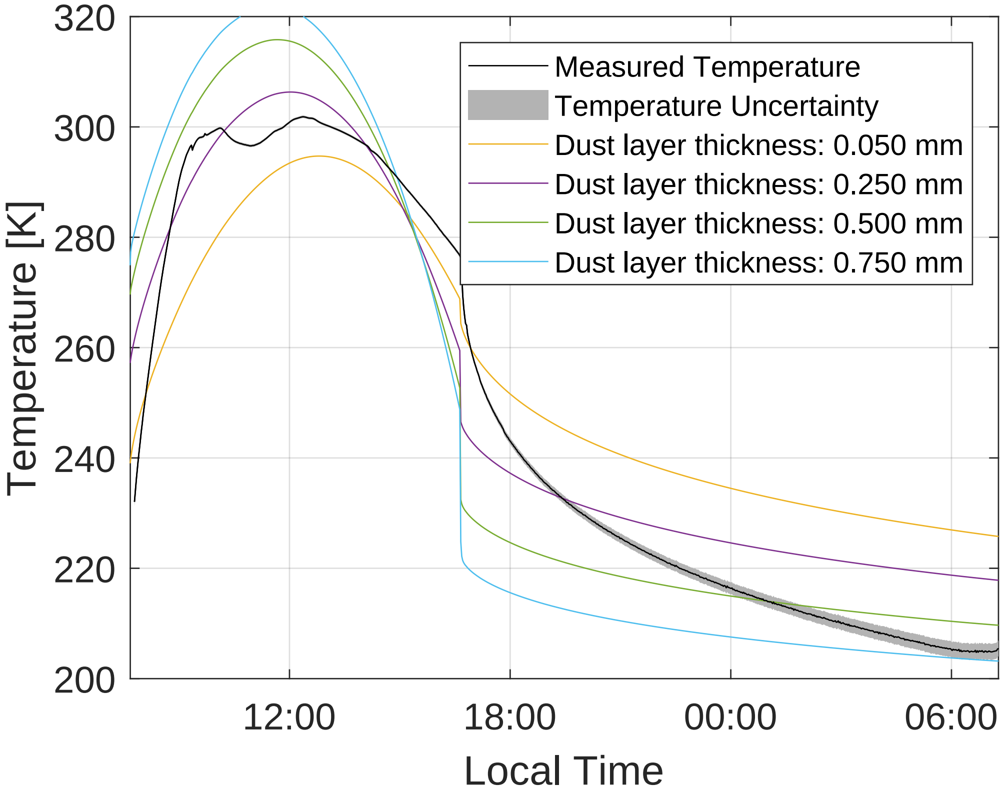
Measured Temperature
Temperature Uncertainty
Dust layer thickness: 0.050 mm
Dust layer thickness: 0.250 mm
Dust layer thickness: 0.500 mm
Dust layer thickness: 0.750 mm
320
300
280
260
240
220
200
Temperature [K]
12:00
18:00
00:00
06:00
Local Time

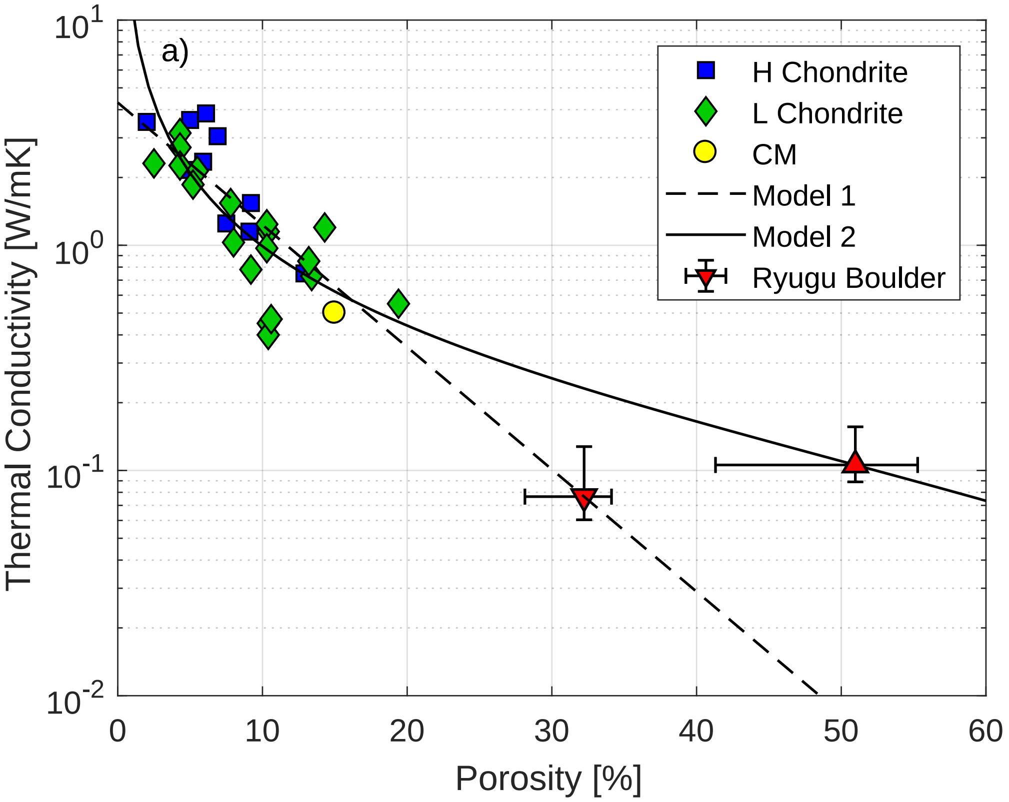

a)
Thermal Conductivity [W/mK]
10^{1}
10^{0}
10^{-1}
10^{-2}
0
10
20
30
40
50
60
Porosity [%]
H Chondrite
L Chondrite
CM
Model 1
Model 2
Ryugu Boulder

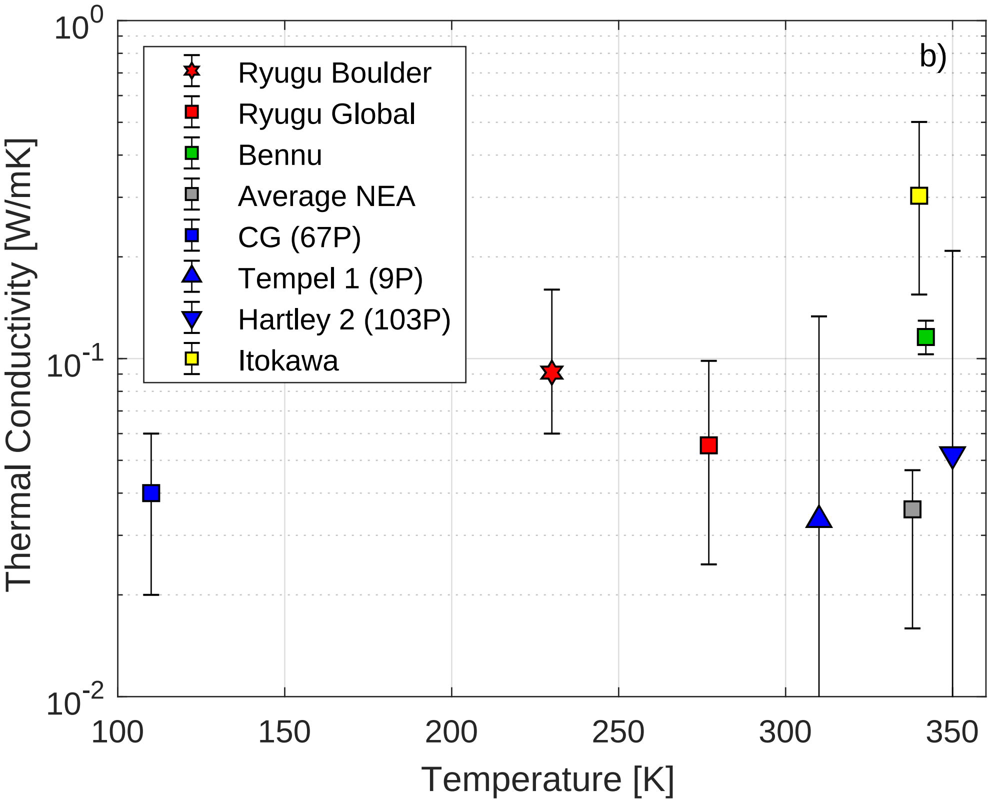
b)
Thermal Conductivity [W/mK]
Temperature [K]
10^0
10^{-1}
10^{-2}
100
150
200
250
300
350
Ryugu Boulder
Ryugu Global
Bennu
Average NEA
CG (67P)
Tempel 1 (9P)
Hartley 2 (103P)
Itokawa